DOI: www.doi.org/10.1109/TMAG.2019.2950614
URL: www.ieeexplore.ieee.org/document/8936605

Cite: J.-L. Guo, L. Quéval, B. Roucaries, L. Vido, L. Liu, F. Trillaud, C. Berriaud, ”Nonlinear current sheet model of electrical machines,” *IEEE Transactions on Magnetics*, vol. 56, no. 1, id. 7502904, Jan. 2020.

Nonlinear Current Sheet Model of Electrical Machines (Extended version)

Jiling Guo[1,2], Loïc Quéval[2], Bastien Roucaries[3], Lionel Vido[3], Li Liu[1], Frederic Trillaud[4], Christophe Berriaud[5]
[1] School of Electrical Engineering, Southwest Jiaotong University, 610031 Chengdu,China
[2] GeePs, UMR CNRS 8507, CentraleSupelec, Univ. Paris-Sud, Univ. Paris-Saclay, Sorbonne Univ., 91192 Gif-sur-Yvette, France
[3] SATIE, CNRS UMR 8029, Univ. of Cergy Pontoise, 95000 Cergy-Pontoise, France
[4] Instituto de Ingeniería, Universidad Nacional Autónoma de México, 04510 CDMX, Mexico
[5] DRF/IRFU/DACM, CEA Saclay, Univ. Paris-Saclay, 91191 Gif-sur-Yvette, France

An incremental improvement of the classical semi-analytical current sheet model of electrical machines is proposed. First, it provides a better description of the current sheets that allows to consider, at the same time, the rotation of the rotor field winding and the time-dependent stator armature windings currents. This derivation is kept generic and the system to be solved is explicitly written in order to facilitate the implementation. Second, a refined iterative scheme that permits to account effectively for the nonlinearity of iron cores is introduced. It is demonstrated that the nonlinear current sheet model is particularly suitable for slotless wound rotor machines, being able to represent both the space harmonics and the saturation of the machine with a fair accuracy and computing speed compared to the nonlinear finite element model.

***Index Terms*—Electrical machine modeling and simulation, semi-analytical model, subdomain model, current sheet model, nonlinear material, slotless machine, air cored machine.**

I. Introduction

THE "CURRENT SHEET MODEL" is a semi-analytical model for the calculation of the magnetic field in an electrical machine. It belongs to the family of "subdomain models" ie. it is based on the formal resolution of Maxwell's equations in each subdomain [2]. Its distinctive feature is to divide the machine into annular subdomains and to model the windings as cylindrical current sheets. The Laplace's equation for the magnetic vector potential $\mathbf{A}$ can then be solved analytically in each subdomain by the classic method of the separation of variables using appropriate boundary and interface conditions. Hugues and Miller pioneered this method in 1977 [3], [4]. At the time, they obtained concise analytical formulas for the field in the rotor core, air gap, stator core and air surrounding the machine. The method was later extended to add the shaft [5], [6], [7], the current sheets space harmonics [8] and the winding thickness [9]. Finally an iterative technique was introduced by Yazdanian *et al.* [5], [6] to account for the nonlinearity of the iron. Despite those improvements, the latest models could not include directly several windings at the same time nor account for the rotation of the rotor.

The following work tackles this problem by expressing the current sheets not only as a classic sum of sines but as a sum of both sines and cosines. As a result, the proposed model can naturally include both the rotation of the rotor field winding and the time-dependent stator armature windings currents. In addition, an iterative scheme improved from [5], [6] is used to take into account the nonlinearity of the iron.

Corresponding authors: L. Quéval (email: loic.queval@centralesupelec.fr) and F. Trillaud (ftrillaudp@pumas.ii.unam.mx).

II. Machine geometry

The current sheet model assumes that the whole machine domain is divided into N concentric annular subdomains. For $\ell \in [1, N]$, the ℓ^{th} subdomain has an inner radius $r_{\ell-1}$, an outer radius r_ℓ and a relative permeability $\mu_{r,\ell}$. The boundary between the ℓ^{th} domain and the $(\ell+1)^{\text{th}}$ domain is a current sheet $K_\ell(\theta)$ located at $r = r_\ell$.

To illustrate how the approach is applied to a specific machine, we considered the slotless wound rotor synchronous machine with concentrated windings shown in Fig. 1. The current sheet model is particularly well suited for this kind of machine, but it has also been used for slotted machines [8]. From the basic assumptions of the model, the windings are described by cylindrical current sheets. Therefore, the whole domain is divided into 7 annular concentric subdomains: the shaft (1), the rotor iron core (2), the rotor air core (3), the air gap (4), the stator air core (5), the stator iron core (6), and the air surrounding the machine (7). The parameters of the machine are the rotor core inner radius r_1, the rotor core outer radius r_2, the field winding radius r_3, the armature winding radius r_4, the stator core inner radius r_5, and the stator core outer radius r_6. The rotor and stator iron core subdomains have a relative permeability larger than 1 which can be either constant in the linear case or depending on the magnetic field in the nonlinear case. The boundary between the rotor air core subdomain (3) and the air gap subdomain (4) is the rotor field winding current sheet $K_3(\theta)$. The boundary between the air gap subdomain (4) and the stator air core subdomain (5) is the stator armature winding current sheet $K_4(\theta)$. The other current sheets are zero.

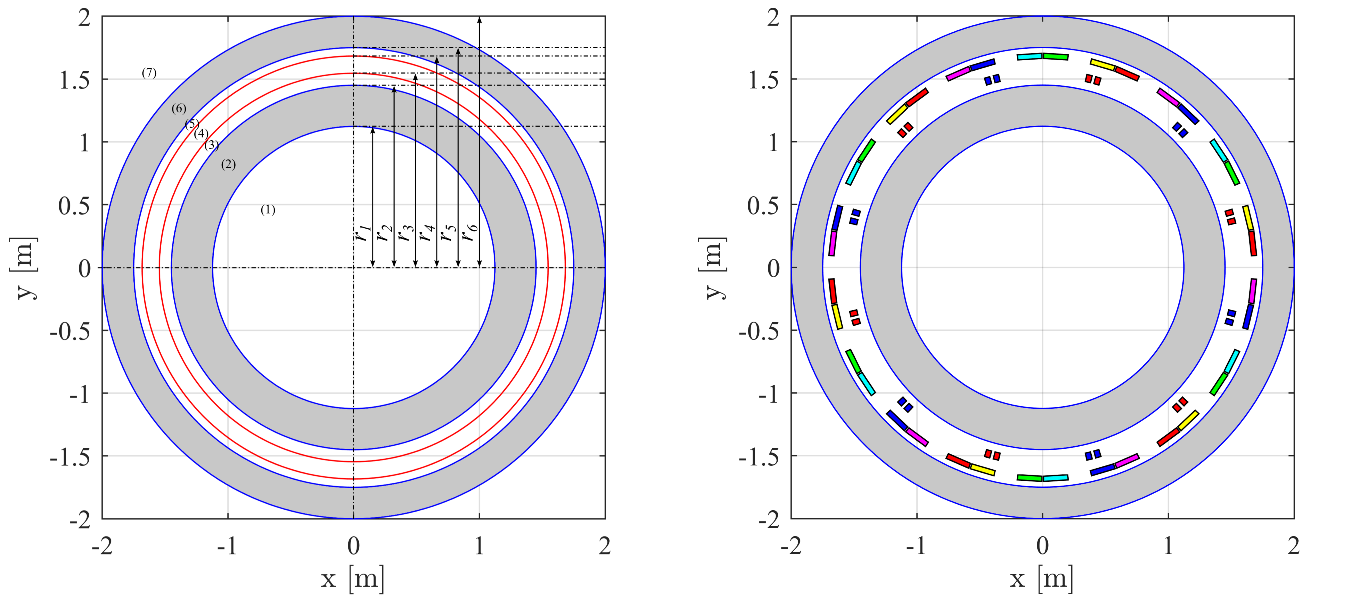

(a) Generic geometry

(b) Specific geometry ($\alpha = 0°$)

Fig. 1. Machine geometry: (a) generic geometry corresponding to the specific machine (b).

III. Modeling

A. Equivalent current sheet $K_\ell(\theta)$

For a machine with P pairs of pole, $K_\ell(\theta)$ is $\frac{2\pi}{P}$-periodic with a mean value equal to zero. Thus, it can be written as a Fourier series,

$$K_\ell(\theta) = \sum_{h=1}^{+\infty} \left[K^s_{\ell,h}\sin(hP\theta) + K^c_{\ell,h}\cos(hP\theta)\right] \quad (1)$$

where $K^s_{\ell,h}$ and $K^c_{\ell,h}$ are Fourier coefficients to be determined from the machine specific geometry.

B. Magnetic vector potential $\mathbf{A}$ in the ℓ^{th} subdomain

In 2-D polar coordinates (neglecting the end effects), the magnetic vector potential $\mathbf{A}$ has only one component along the z-axis and depends only on r and θ coordinates. The resulting scalar potential $A_z(r,\theta)$ is solution of Laplace's equation. Using the method of the separation of variables in the ℓ^{th} annular subdomain and considering the current sheets to be expressed as (1), the scalar potential $A_{z,\ell}(r,\theta)$ reduces to,

$$\begin{aligned} A_{z,\ell}(r,\theta) = \sum_{h=1}^{+\infty} \Big[&\left(a_{\ell,h}r^{hP} + b_{\ell,h}r^{-hP}\right)\sin(hP\theta) \\ &+ \left(c_{\ell,h}r^{hP} + d_{\ell,h}r^{-hP}\right)\cos(hP\theta)\Big] \end{aligned} \quad (2)$$

where $a_{\ell,h}$, $b_{\ell,h}$, $c_{\ell,h}$ and $d_{\ell,h}$ are coefficients to be determined.

C. Magnetic flux density $\mathbf{B}$ and magnetic field strength $\mathbf{H}$ in the ℓ^{th} subdomain

In 2-D polar coordinates, the magnetic flux density components are obtained from the relation $\mathbf{B} = \nabla \times \mathbf{A}$ as,

$$\begin{cases} B_r = \dfrac{1}{r}\dfrac{\partial A_z}{\partial \theta} \\ B_\theta = -\dfrac{\partial A_z}{\partial r} \end{cases} \quad (3)$$

By substituting (2) into (3), the magnetic flux density in each subdomain ℓ is given by,

$$\begin{cases} B_{r,\ell}(r,\theta) = & \sum\limits_{h=1}^{+\infty} \big[(a_{\ell,h}r^{hP-1} + b_{\ell,h}r^{-hP-1})hP\cos(hP\theta) \\ & \quad -(c_{\ell,h}r^{hP-1} + d_{\ell,h}r^{-hP-1})hP\sin(hP\theta)\big] \\ B_{\theta,\ell}(r,\theta) = & \sum\limits_{h=1}^{+\infty} \big[(-a_{\ell,h}r^{hP-1} + b_{\ell,h}r^{-hP-1})hP\sin(hP\theta) \\ & \quad +(-c_{\ell,h}r^{hP-1} + d_{\ell,h}r^{-hP-1})hP\cos(hP\theta)\big] \end{cases} \quad (4)$$

and, subsequently, the magnetic field strength can be obtained from $\mathbf{H} = \mu^{-1}\mathbf{B}$ for each subdomain ℓ with permeability μ_ℓ,

$$\begin{cases} H_{r,\ell}(r,\theta) = & \sum\limits_{h=1}^{+\infty} \big[(a_{\ell,h}r^{hP-1} + b_{\ell,h}r^{-hP-1})\mu_\ell^{-1}hP\cos(hP\theta) \\ & \quad -(c_{\ell,h}r^{hP-1} + d_{\ell,h}r^{-hP-1})\mu_\ell^{-1}hP\sin(hP\theta)\big] \\ H_{\theta,\ell}(r,\theta) = & \sum\limits_{h=1}^{+\infty} \big[(-a_{\ell,h}r^{hP-1} + b_{\ell,h}r^{-hP-1})\mu_\ell^{-1}hP\sin(hP\theta) \\ & \quad +(-c_{\ell,h}r^{hP-1} + d_{\ell,h}r^{-hP-1})\mu_\ell^{-1}hP\cos(hP\theta)\big] \end{cases} \quad (5)$$

D. Boundary and interface conditions

At $r = 0$ ($\ell = 1$), the boundary condition is,

$$A_{z,1}(0,\theta) = 0, \qquad \forall\theta \quad (6)$$

At $r = r_\ell$ $(1 \leq \ell < N)$, the interface condition is,

$$\begin{cases} B_{r,\ell+1}(r_\ell,\theta) - B_{r,\ell}(r_\ell,\theta) = 0 \\ H_{\theta,\ell+1}(r_\ell,\theta) - H_{\theta,\ell}(r_\ell,\theta) = K_\ell(\theta), \end{cases} \quad \forall\theta \tag{7}$$

At $r = +\infty$ $(\ell = N)$, the boundary condition is,

$$A_{z,N}(+\infty,\theta) = 0, \quad \forall\theta \tag{8}$$

Using (1)-(5), the boundary and interface conditions (6)-(8) can be rewritten as a set of $4N$ equations that must be respected for each harmonic h,

$$\begin{cases} b_{1,h} = 0 \\ d_{1,h} = 0 \\ \vdots \\ (a_{\ell+1,h} r_\ell^{hP-1} + b_{\ell+1,h} r_\ell^{-hP-1}) \\ \qquad - (a_{\ell,h} r_\ell^{hP-1} + b_{\ell,h} r_\ell^{-hP-1}) = 0 \\ (c_{\ell+1,h} r_\ell^{hP-1} + d_{\ell+1,h} r_\ell^{-hP-1}) \\ \qquad - (c_{\ell,h} r_\ell^{hP-1} + d_{\ell,h} r_\ell^{-hP-1}) = 0 \\ (-a_{\ell+1,h} r_\ell^{hP-1} + b_{\ell+1,h} r_\ell^{-hP-1}) \mu_{\ell+1}^{-1} hP \\ \qquad - (-a_{\ell,h} r_\ell^{hP-1} + b_{\ell,h} r_\ell^{-hP-1}) \mu_\ell^{-1} hP = K_{\ell,h}^s \\ (-c_{\ell+1,h} r_\ell^{hP-1} + d_{\ell+1,h} r_\ell^{-hP-1}) \mu_{\ell+1}^{-1} hP \\ \qquad - (-c_{\ell,h} r_\ell^{hP-1} + d_{\ell,h} r_\ell^{-hP-1}) \mu_\ell^{-1} hP = K_{\ell,h}^c \\ \vdots \\ a_{N,h} = 0 \\ c_{N,h} = 0 \end{cases} \tag{9}$$

The system (9) can finally be written as a generic system (10) of the form $\mathbf{Rx} = \mathbf{b}$. Being generic and explicit, the implementation of the current sheet model is straightforward [10].

E. Linear model

In the linear case, the permeability μ_ℓ is independent of the magnetic field, and R is constant. The coefficients $a_{\ell,h}$, $b_{\ell,h}$, $c_{\ell,h}$ and $d_{\ell,h}$ for $\ell = \{1, \cdots, N\}$ are obtained by solving numerically the linear system (10) for which R is considered constant. In the present case, R is ill-conditioned for which classical methods based on direct solver are not suitable even with the use of preconditioners. In this particular case, a linear least square solver proved to be satisfactory.

Inserting these coefficients into (2) and (4), one finds the expressions for the potential $A_{z,\ell}$ and the components of the magnetic flux density $B_{r,\ell}$ and $B_{\theta,\ell}$ in the ℓ^{th} subdomain.

F. Nonlinear model

In the nonlinear case, the permeability μ_ℓ is a function of the magnetic field, and R is not constant anymore. In the current sheet model, the permeability μ_ℓ is modeled as uniform over the whole ℓ^{th} subdomain. If this is not a limitation in the linear case, it becomes problematic when considering a nonlinear BH curve for the iron. Indeed, to preserve the accuracy of the model one should select an effective permeability that can represent well the non-uniformly magnetized core. Here, the fixed-point iteration procedure with numerical damping depicted in Fig. 2 has been implemented. Inspired by [5], [6], [11], this improved scheme computes the effective rotor permeability as the minimum of the permeability along the mean radius of the domain. Note that at each iteration, the μ_ℓ of the subdomain ℓ is fixed. This allows us to solve a linear problem, where the different harmonics can be simply added.

IV. RESULTS

Because of its underlying modeling hypotheses, the current sheet model is naturally adapted to slotless wound rotor electrical machine. As an example, we investigate here the performance of the 12-pole 3-phase synchronous machine with concentrated windings shown in Fig 1. Such a structure has been recently proposed for multi-MW fully superconducting wind turbine generators [12], [13]. The suppression of magnetic teeth is often considered for superconducting machines to cope with their large magnetic field (up to several Tesla), with the difficulty of winding superconducting materials and to simplify the cooling system. The machine parameters are summarized in Table I. The iron relative permeability as a function of the norm of the magnetic flux density is plotted in Fig. 3. For the current sheet model, 13 harmonic terms are included. For validation purpose, the results are compared to a nonlinear 2-D finite element (FE) model carried out in COMSOL Multiphysics.

TABLE I
PARAMETERS OF THE 12-POLE 3-PHASE SYNCHRONOUS MACHINE

Symbol	Parameter	Value
r_1	rotor core inner radius	1.320 m
r_2	rotor core outer radius	1.470 m
r_3	field winding radius	1.546 m
r_4	armature windings radius	1.683 m
r_5	stator core inner radius	1.750 m
r_6	stator core outer radius	2.000 m
μ_1	shaft permeability	μ_0
μ_2	rotor core permeability	$\mu_0\mu_r(\lvert\mathbf{B}\rvert)$
μ_3	rotor air core permeability	μ_0
μ_4	air-gap permeability	μ_0
μ_5	stator air core permeability	μ_0
μ_6	stator core permeability	$\mu_0\mu_r(\lvert\mathbf{B}\rvert)$
μ_7	outer air permeability	μ_0
K_1		0
K_2		0
K_3	field winding	$K_3(\theta)$
K_4	armature windings	$K_4(\theta)$
K_5		0
K_6		0
K_7		0
P	number of pole pairs	6
m	number of phases	3
h_f	field coil height	0.057 m
w_f	field coil width	0.042 m
θ_{1f}	field coil width elec. angle	0.163 rad
θ_{2f}	field coil aperture elec. angle	2.703 rad
h_a	armature coil height	0.041 m
w_a	armature coil width	0.194 m
θ_{1a}	armature coil width elec. angle	0.692 rad
θ_{2a}	armature coil aperture elec. angle	0.664 rad
L_{eff}	effective length	1.540 m
N_a	armature windings nb of turns	120
N_f	field winding nb of turns	100
r_{Te}	radius for evaluation of field and torque	1.619 m

$$
\underbrace{\begin{bmatrix}
0\ 1\ 0\ 0\ 0\ 0\ 0\ 0 & & & & \\
0\ 0\ 0\ 1\ 0\ 0\ 0\ 0 & & & \mathbf{0} & \\
R_{3,1} & & & & \\
& \ddots & & & \\
& & R_{4(\ell-1)+3,4(\ell-1)+1} & & \\
& & & \ddots & \\
& & & & R_{4(N-2)+3,4(N-2)+1} \\
& \mathbf{0} & & & 0\ 0\ 0\ 0\ 1\ 0\ 0\ 0 \\
& & & & 0\ 0\ 0\ 0\ 0\ 0\ 1\ 0
\end{bmatrix}}_{\mathbf{R}_{4N\times 4N}}
\times
\underbrace{\begin{bmatrix} x_1 \\ x_2 \\ \vdots \\ x_{4(\ell-1)+1} \\ \vdots \\ x_{N-1} \\ x_N \end{bmatrix}}_{\mathbf{x}_{4N\times 1}}
=
\underbrace{\begin{bmatrix} 0 \\ 0 \\ K_3 \\ \vdots \\ K_{4(\ell-1)+3} \\ \vdots \\ K_{4(N-2)+3} \\ 0 \\ 0 \end{bmatrix}}_{\mathbf{b}_{4N\times 1}}
$$

$$
R_{4(\ell-1)+3,4(\ell-1)+1} = \begin{bmatrix}
-r_\ell^{hP} & -r_\ell^{-hP} & 0 & 0 & r_\ell^{hP} & r_\ell^{-hP} & 0 & 0 \\
0 & 0 & -r_\ell^{hP} & -r_\ell^{-hP} & 0 & 0 & r_\ell^{hP} & r_\ell^{-hP} \\
\dfrac{r_\ell^{hP}}{\mu_\ell} & -\dfrac{r_\ell^{-hP}}{\mu_\ell} & 0 & 0 & -\dfrac{r_\ell^{hP}}{\mu_{\ell+1}} & \dfrac{r_\ell^{-hP}}{\mu_{\ell+1}} & 0 & 0 \\
0 & 0 & \dfrac{r_\ell^{hP}}{\mu_\ell} & -\dfrac{r_\ell^{-hP}}{\mu_\ell} & 0 & 0 & -\dfrac{r_\ell^{hP}}{\mu_{\ell+1}} & \dfrac{r_\ell^{-hP}}{\mu_{\ell+1}}
\end{bmatrix}_{4\times 8}
$$

$$
x_{4(\ell-1)+1} = \begin{bmatrix} a_{\ell,h} \\ b_{\ell,h} \\ c_{\ell,h} \\ d_{\ell,h} \end{bmatrix}_{4\times 1} \qquad K_{4(\ell-1)+3} = \frac{1}{hP}\begin{bmatrix} 0 \\ 0 \\ K^s_{\ell,h} r_\ell \\ K^c_{\ell,h} r_\ell \end{bmatrix}_{4\times 1} \tag{10}
$$

where $1 \leq \ell < N$.

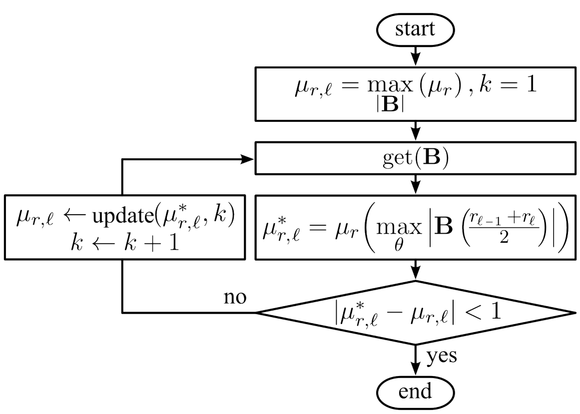

Fig. 2. Iterative scheme to determine the effective subdomain relative permeabilities μ_ℓ in the nonlinear case. The update operator designates the numerical damping.

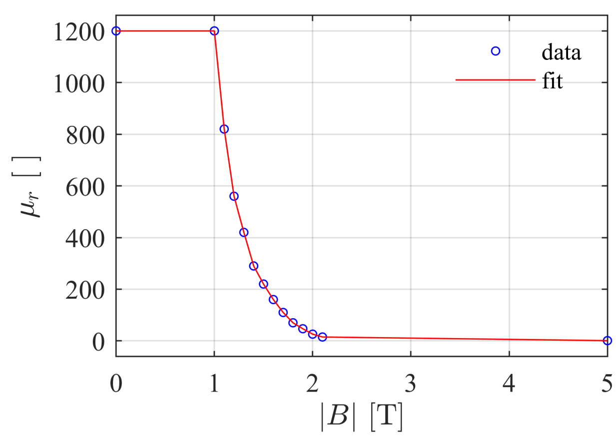

Fig. 3. Relative permeability μ_r of the rotor and stator core as a function of the norm of the magnetic flux density. (B, H) = [(1.0, 663), (1.1, 1067), (1.2, 1705), (1.3, 2463), (1.4, 3841), (1.5, 5425), (1.6, 7957), (1.7, 12298), (1.8, 20462), (1.9, 32169), (2.0, 61213), (2.1, 111408), (2.3, 500000), (2.6, 1500000), (5, 3978900)]. B in T, H in A·m^{-1}.

A. Equivalent current sheets

a) Field winding K_3: For the specific field winding arrangement of Fig. 1, $K_3(\theta)$ is given by (see appendix A for its derivation),

$$
\begin{aligned}
K_3(\theta) &= \sum_{\substack{h=1 \\ h \text{ odd}}}^{+\infty} \left[K^s_{3,h}\sin(hP\theta) + K^c_{3,h}\cos(hP\theta)\right] \\
K^s_{3,h} &= \frac{8N_f i_f}{\pi w_f h}\sin\left(\frac{\theta_{1f}+\theta_{2f}}{2}h\right)\sin\left(\frac{\theta_{1f}}{2}h\right)\cos(hP\alpha) \\
K^c_{3,h} &= -\frac{8N_f i_f}{\pi w_f h}\sin\left(\frac{\theta_{1f}+\theta_{2f}}{2}h\right)\sin\left(\frac{\theta_{1f}}{2}h\right)\sin(hP\alpha)
\end{aligned} \tag{11}
$$

where α is the rotor mechanical angle, N_f is the number of turns of the rotor winding, i_f is the instantaneous field coil current, θ_{1f} is the coil width electrical angle, θ_{2f} is the coil aperture electrical angle and w_f is the coil width.

b) Armature windings K_4: Similarly, for the specific armature winding arrangement of Fig. 1, $K_4(\theta)$ is given by (see appendix B for its derivation),

$$K_4(\theta) = \sum_{h=1}^{+\infty} \left[K_{4,h}^s \sin(hP\theta) + K_{4,h}^c \cos(hP\theta)\right]$$

$$K_{4,h}^s = \frac{4N_a}{\pi w_a h} \sin\left(\frac{\theta_{1a}+\theta_{2a}}{2}h\right) \sin\left(\frac{\theta_{1a}}{2}h\right) \times \left[i_a + i_b \cos\left(h\frac{2\pi}{3}\right) + i_c \cos\left(h\frac{4\pi}{3}\right)\right]$$

$$K_{4,h}^c = -\frac{4N_a}{\pi w_a h} \sin\left(\frac{\theta_{1a}+\theta_{2a}}{2}h\right) \sin\left(\frac{\theta_{1a}}{2}h\right) \times \left[i_b \sin\left(h\frac{2\pi}{3}\right) + i_c \sin\left(h\frac{4\pi}{3}\right)\right] \tag{12}$$

where N_a is the number of turns of the armature windings, (i_a, i_b, i_c) are the instantaneous 3-phase currents, θ_{1a} is the coil width electrical angle, θ_{2a} is the coil aperture electrical angle and w_a is the coil width.

B. Load condition

For the load condition, the following parameters are used: $i_f = 5.03$ kA, $i_a = -1.53$ kA, $i_b = 2.465$ kA, $i_c = -0.935$ kA, $\alpha = -15^o$. The magnetic flux density in the air gap is plotted in Fig. 4. Fig. 5 shows the magnetic flux density distribution in the whole domain. In the linear case, the agreement between the current sheet model and the FE model is very good. In the nonlinear case, the agreement is good for the field in the air gap and fair for the field distribution. The discrepancy is mainly attributed to the impossibility of modeling the azimuthal variation of μ_ℓ for the current sheet model. The computation time for the nonlinear current sheet model is about 1.3 s (roughly 100 ms per iteration, <15 iterations) on an i7-5600 CPU @2.60 Ghz, 16 GB RAM. This is about 5 times faster than the nonlinear FE model, using symmetries to reduce the mesh to 9220 elements. Note that an efficient implementation of the current sheet model could lead to an even lower computing time [14].

V. Conclusion

In comparison to previous current sheet models, the present derivation sets itself apart by its genericity. It accounts simultaneously for the rotor rotation and the time-dependent stator currents. In addition, the nonlinearity of the cores is included thanks to an iterative procedure. It provides the end user with a simple model that can be quickly implemented in any freely-available programing languages to carry out pre-design and optimization studies of slotless wound rotor electrical machines. It is adapted to a wide range of designs, including multiphase machines with multi-layer distributed or concentrated windings.

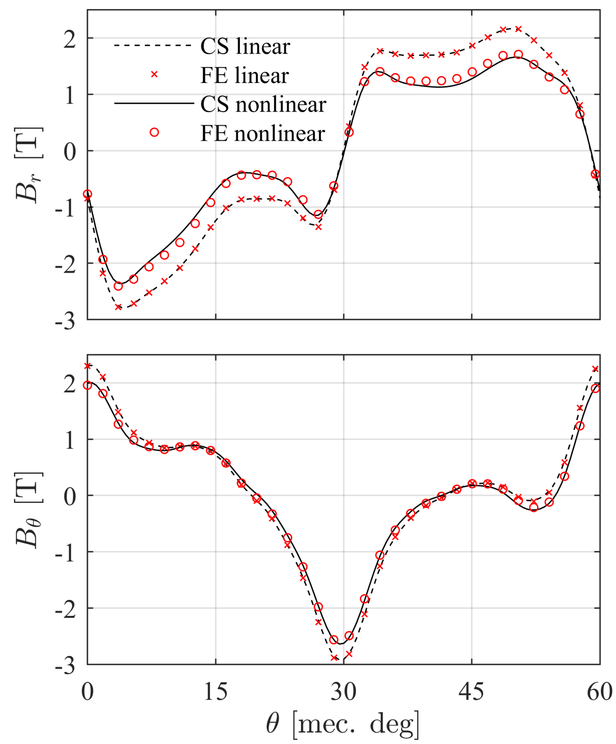

Fig. 4. Comparison of the air-gap (top) radial and (bottom) azimuthal components of the magnetic flux density for the current sheet (CS) model and the finite element (FE) model ($r = r_{Te}$).

Appendix A
Field winding equivalent current sheet

For a machine with P pole pairs, the current sheets $K_\ell(\theta)$ are $\frac{2\pi}{P}$-periodic. It is convenient to define the electrical angle θ_e from the mechanical angle θ by the relation $\theta_e = P\theta$. The current sheets can then be expressed as a Fourier series as follows,

$$\begin{aligned} K_\ell(\theta_e) &= \frac{a_{\ell,0}}{2} + \sum_{h=1}^{+\infty} \left[a_{\ell,h} \cos(h\theta_e) + b_{\ell,h} \sin(h\theta_e)\right] \\ a_{\ell,0} &= \frac{1}{\pi} \int_{-\pi}^{\pi} K_\ell(\theta_e) d\theta_e \\ a_{\ell,h} &= \frac{1}{\pi} \int_{-\pi}^{\pi} K_\ell(\theta_e) \cos(h\theta_e) d\theta_e \\ b_{\ell,h} &= \frac{1}{\pi} \int_{-\pi}^{\pi} K_\ell(\theta_e) \sin(h\theta_e) d\theta_e \end{aligned} \tag{13}$$

The field winding is made of racetrack coils connected in series and assembled as shown in Fig. 6(a). It is modeled by the current sheet $K_3(\theta_e)$ located at the winding mean winding radius r_3 and shown in Fig. 6(b).

$K_f(\theta_e)$ is an odd function, so $a_{3,0} = 0$ and $a_{3,h} = 0$. From

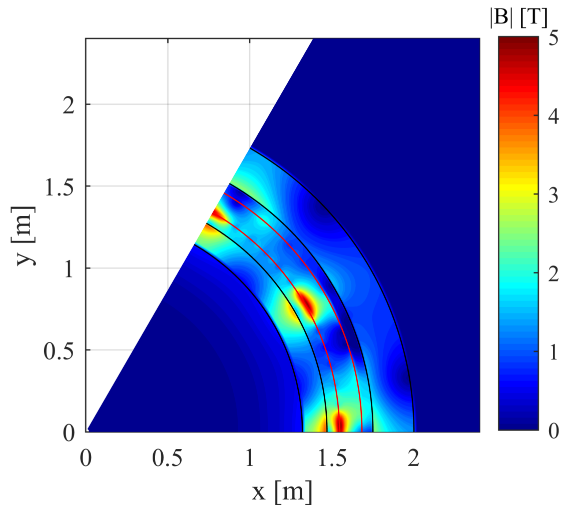

(a) CS nonlinear model

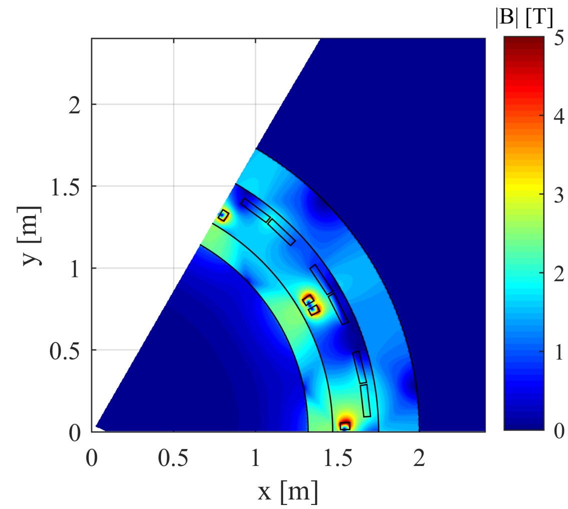

(b) FE nonlinear

Fig. 5. Comparison of the magnetic flux density distribution for the current sheet (CS) model and the finite element (FE) model (load condition at $t = 0$ s).

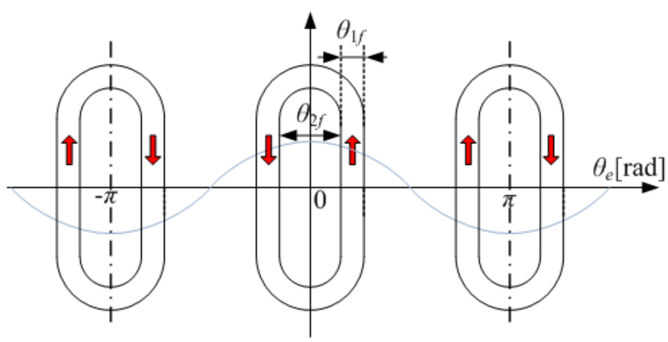

(a) Geometry

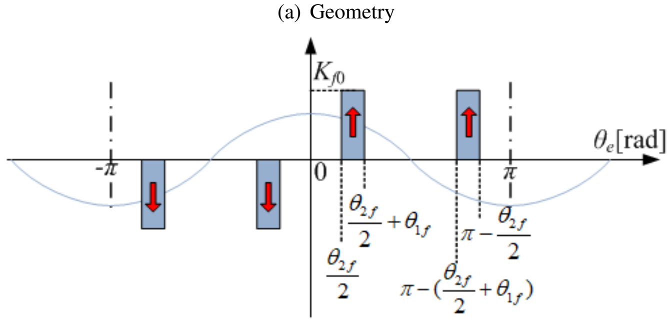

(b) Equivalent current sheet

Fig. 6. Rotor field winding ($\alpha = 0$).

(13) with the help of Fig. 6(b),

$$\begin{cases} K_3(\theta_e) = \displaystyle\sum_{\substack{h=1 \\ h \text{ odd}}}^{+\infty} b_{3,h} \sin(h\theta_e) \\ b_{3,h} = \dfrac{8K_{f0}}{\pi h} \sin\left(\dfrac{\theta_{1f}+\theta_{2f}}{2} h\right) \sin\left(\dfrac{\theta_{1f}}{2} h\right) \\ K_{f0} = \dfrac{N_f i_f}{w_f} \end{cases} \tag{14}$$

where N_f is the number of turns, i_f is the instantaneous current of the field winding and $w_f = r_3\theta_{1f}/P$ is the coil width. To include the rotation, (14) is expressed as a function of the mechanical angle θ and translated by the rotor mechanical angle α,

$$K_3(\theta) = \sum_{\substack{h=1 \\ h \text{ odd}}}^{\infty} b_{3,h} \sin(hP(\theta - \alpha)) \tag{15}$$

Using trigonometric relations,

$$\begin{aligned} K_3(\theta) &= \sum_{\substack{h=1 \\ h \text{ odd}}}^{+\infty} \left[K_{3,h}^s \sin(hP\theta) + K_{3,h}^c \cos(hP\theta)\right] \\ K_{3,h}^s &= \frac{8K_{f0}}{\pi h} \sin\left(\frac{\theta_{1f}+\theta_{2f}}{2} h\right) \sin\left(\frac{\theta_{1f}}{2} h\right) \cos(hP\alpha) \\ K_{3,h}^c &= -\frac{8K_{f0}}{\pi h} \sin\left(\frac{\theta_{1f}+\theta_{2f}}{2} h\right) \sin\left(\frac{\theta_{1f}}{2} h\right) \sin(hP\alpha) \\ K_{f0} &= \frac{N_f i_f}{w_f} \end{aligned} \tag{16}$$

Appendix B
Armature Windings Equivalent Current Sheet

The 3-phase armature windings are made of racetrack coils assembled as shown in Fig. 7(a). They are modeled by a current sheet $K_4(\theta)$ located at the winding mean windings radius r_4 and shown in Fig. 7(b). $K_4(\theta)$ is obtained by summing $K_a(\theta)$, $K_b(\theta)$ and $K_c(\theta)$.

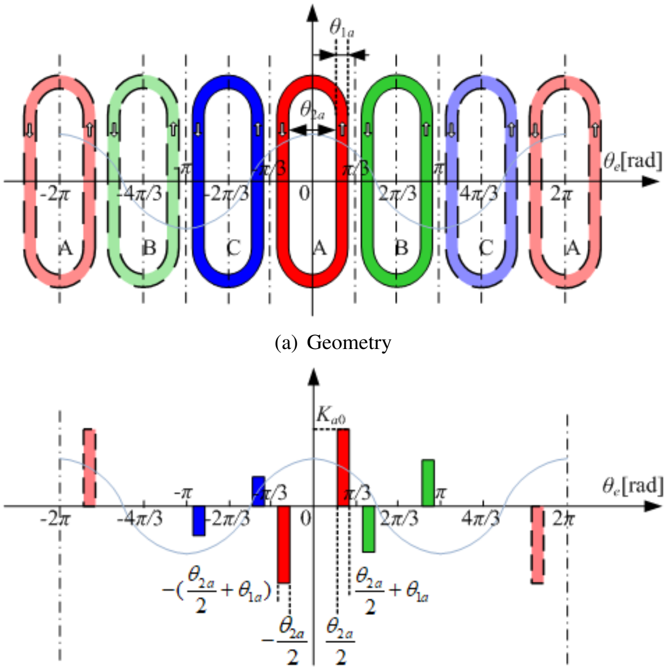

(a) Geometry

(b) Equivalent current sheet

Fig. 7. Stator armature windings.

$K_a(\theta_e)$ is an odd function, so $a_{a,0} = 0$ and $a_{a,h} = 0$. From (13) with the help of Fig. 7(b),

$$
\begin{cases}
K_a(\theta_e) = \sum_{h=1}^{+\infty} b_{a,h} \sin(h\theta_e) \\
b_{a,h} = \frac{4K_{a0}}{\pi h} \sin\left(\frac{\theta_{1a}+\theta_{2a}}{2} h\right) \sin\left(\frac{\theta_{1a}}{2} h\right) \\
K_{a0} = \frac{N_a i_a}{w_a}
\end{cases}
\tag{17}
$$

where N_a is the number of turns, i_a is the instantaneous current of the phase a and $w_a = r_4\theta_{1a}/P$ is the coil width. $K_b(\theta_e)$ and $K_c(\theta_e)$ are obtained by translation of $K_a(\theta_e)$ by $\frac{2\pi}{3}$ and $\frac{4\pi}{3}$, respectively,

$$
\begin{cases}
K_b(\theta_e) = \sum_{h=1}^{+\infty} b_{b,h} \sin\left(h\left(\theta_e - \frac{2\pi}{3}\right)\right) \\
b_{b,h} = \frac{4K_{b0}}{\pi h} \sin\left(\frac{\theta_{1a}+\theta_{2a}}{2} h\right) \sin\left(\frac{\theta_{1a}}{2} h\right) \\
K_{b0} = \frac{N_a i_b}{w_a}
\end{cases}
\tag{18}
$$

$$
\begin{cases}
K_c(\theta_e) = \sum_{h=1}^{+\infty} b_{c,h} \sin\left(h\left(\theta_e - \frac{4\pi}{3}\right)\right) \\
b_{c,h} = \frac{4K_{c0}}{\pi h} \sin\left(\frac{\theta_{1a}+\theta_{2a}}{2} h\right) \sin\left(\frac{\theta_{1a}}{2} h\right) \\
K_{c0} = \frac{N_a i_c}{w_a}
\end{cases}
\tag{19}
$$

where i_b and i_c are the instantaneous currents of the phase b and c. $K_4(\theta_e)$ is obtained, as a function of the mechanical angle, by using trigonometric relations and by summing $K_a(\theta_e)$, $K_b(\theta_e)$ and $K_c(\theta_e)$,

$$
\begin{aligned}
K_4(\theta) &= \sum_{h=1}^{+\infty} \left[K^s_{abc,h} \sin(hP\theta) + K^c_{abc,h} \cos(hP\theta)\right] \\
K^s_{4,h} &= \frac{4}{\pi h} \sin\left(\frac{\theta_{1a}+\theta_{2a}}{2} h\right) \sin\left(\frac{\theta_{1a}}{2} h\right) \\
&\quad \times \left[K_{a0} + K_{b0}\cos\left(h\frac{2\pi}{3}\right) + K_{c0}\cos\left(h\frac{4\pi}{3}\right)\right] \\
K^c_{4,h} &= -\frac{4}{\pi h} \sin\left(\frac{\theta_{1a}+\theta_{2a}}{2} h\right) \sin\left(\frac{\theta_{1a}}{2} h\right) \\
&\quad \times \left[K_{b0}\sin\left(h\frac{2\pi}{3}\right) + K_{c0}\sin\left(h\frac{4\pi}{3}\right)\right] \\
K_{a0} &= \frac{N_a i_a}{w_a}, \quad K_{b0} = \frac{N_a i_b}{w_a}, \quad K_{c0} = \frac{N_a i_c}{w_a}
\end{aligned}
\tag{20}
$$

Acknowledgment

This work was supported by the grants: EolSupra20 project ANR-10-LABX-0040-LaSIPS, Chinese Scholarship Council and Fundamental Research Funds for the Centrale Universities under grants 2682018CX18, DGAPA-UNAM PAPIIT-2019 (#IN107119) and Programa de Apoyos para la Superación del Personal Académico of the UNAM (PASPA-DGAPA 2019).

References

[1] B.L.J. Gysen, K.J. Meessen, J.J.H. Paulides, E.A. Lomonova, "General formulation of the electromagnetic field distribution in machines and devices using fourier analysis," *IEEE Trans. on Magnetics*, vol. 46, no. 1, pp. 39-52, 2010.

[2] E. Devillers, J. Le Besnerais, T. Lubin, M. Hecquet, J.-P. Lecointe, "A review of subdomain modeling techniques in electrical machines: performances and applications," *22th Intl. Conf. Elec. Machines ICEM2016*, pp. 86-92, Lausanne, Switzerland, 2016.

[3] A. Hughes, T.J.E. Miller, "Analysis of fields and inductances in air-cored and iron-cored synchronous machines," *Proc. Inst. Elect. Eng.*, vol. 124, no. 2, pp. 121-126, 1977.

[4] T.J.E. Miller, A. Hughes, "Comparative design and performance analysis of air-cored and iron-cored synchronous machines," *Proc. Inst. Elect. Eng.*, vol. 124, no. 2, pp. 127–132, 1977.

[5] P. Elhaminia, M. Yazdanian, M.R. Zolghadri, M. Fardmanesh, "An analytical approach for optimal design of rotor iron for superconducting synchronous machine," *37th Annual Conf. IEEE Industrial Electronics Society IECON2011*, Melbourne, Australia, pp. 1741–1745, 2011.

[6] M. Yazdanian, P. Elhaminia, M.R. Zolghadri, M. Fardmanesh, "Analytical modeling of magnetic flux in superconducting synchronous machine," *IEEE Trans. on Applied Superconductivity*, vol. 23, no. 1, id. 5200406, 2013.

[7] W. Zhang, D. Xia, D. Zhang, G. Zhang, "Parameter design by a novel method and optimization of the field coil for a 500 kW air-gap HTS generator," *IEEE Trans. on Applied Superconductivity*, vol. 24, no. 3, id. 5201704, 2014.

[8] J.R. Bumby, *Superconducting Rotating Electrical Machines*. Oxford, U.K.: Clarendon, 1983.
[9] S. Safi, J. Bumby, "Analysis of magnetic fields in the slotted structure of a superconducting AC generator," *Proc. Inst. Elect. Eng.*, vol. 139, no. 5, pp. 411–422, 1992.
[10] CS model, 2019. [Online]. Available: https://github.com/lqueval/CS. [Accessed Oct. 28, 2019].
[11] Z. Djelloul-Khedda, K. Boughrara, F. Dubas, R. Ibtiouen, "Nonlinear analytical prediction of magnetic field and electromagnetic performances in switched reluctance machines," *IEEE Trans. on Magnetics*, vol. 53, no. 7, pp. 1-11, 2017.
[12] Y. Terao, M. Sekino, H. Ohsaki, "Electromagnetic design of 10 MW class fully superconducting wind turbine generators," *IEEE Trans. on Applied Superconductivity*, vol. 22, no. 3, pp. 5201904, 2012.
[13] T.-K. Hoang, L. Queval, C. Berriaud, L. Vido, "Design of a 20 MW fully superconducting wind turbine generator to minimize the levelized cost of energy," *IEEE Trans. on Applied Superconductivity*, vol. 28, no. 4, pp. 1-4, 2018.
[14] A. Gilson, S. Tavernier, F. Dubas, D. Depernet, C. Espanet, M.M. Technologies, "2-D analytical subdomain model for high speed permanent-magnet machines," *18th Intl. Conf. Elec. Machines and Systems ICEMS2015*, pp. 1508-1514, Pattaya, Thailand, 2015.